SUPPLEMENTARY INFORMATION
On electrically tunable stacking domains and ferroelectricity in moiré superlattices

Daniel Bennett[1] and Benjamin Remez[1]

[1]*Theory of Condensed Matter, Cavendish Laboratory, Department of Physics, J J Thomson Avenue, Cambridge CB3 0HE, United Kingdom*

(Dated: November 11, 2021)

SUPPLEMENTARY NOTE 1: PHYSICAL MODEL

Twistronics

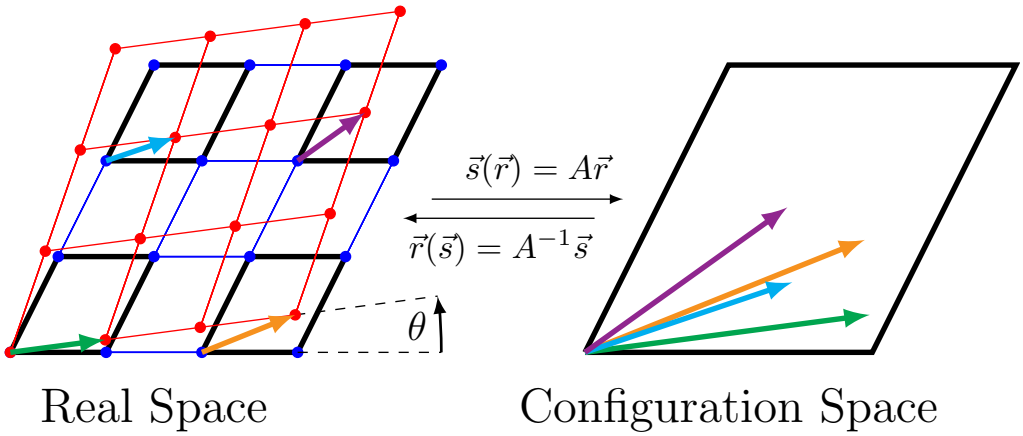

SUPPLEMENTARY FIG 1: Sketch of the mapping between real space and configuration space. On the left is a 3×3 section of a moiré superlattice with twist angle θ. The positions $\mathbf{r}$ are mapped into configuration space via the operator $A = (I - R_\theta^{-1})$, modulo a primitive unit cell. The vectors $\mathbf{s}$ are shown for the four highlighted cells.

A twisted bilayer system is composed of two layers with a relative twist angle θ between them, which we call the reference (r) and twisted (t) layers, respectively. The lattice vectors of the reference layer and the twisted layer are

$$\begin{aligned} \mathbf{a}_{\mathrm{r},1} &= a\begin{bmatrix}1\\0\end{bmatrix}, \qquad \mathbf{a}_{\mathrm{r},2} = \frac{a}{2}\begin{bmatrix}1\\\sqrt{3}\end{bmatrix}, \\ \mathbf{a}_{\mathrm{t},1} &= R_\theta \mathbf{a}_{\mathrm{r},1}, \qquad \mathbf{a}_{\mathrm{t},2} = R_\theta \mathbf{a}_{\mathrm{r},2} \end{aligned} \tag{1}$$

respectively, where a is the monolayer lattice constant and $R_\theta = \begin{bmatrix}\cos(\theta) & -\sin(\theta)\\ \sin(\theta) & \cos(\theta)\end{bmatrix}$. For a general θ, the two layers are incommensurate, i.e. they form a supercell which is infinitely large. If the two layers form a commensurate supercell we can define supercell lattice vectors $\mathbf{L}_i$ as a linear combinations of the lattice vectors of either layer:

$$\begin{aligned} \mathbf{L}_1 &= p\mathbf{a}_{\mathrm{r},1} + q\mathbf{a}_{\mathrm{r},2} \\ &= \bar{p}\mathbf{a}_{\mathrm{t},1} + \bar{q}\mathbf{a}_{\mathrm{t},2} = \bar{p}R_\theta \mathbf{a}_{\mathrm{r},1} + \bar{q}R_\theta \mathbf{a}_{\mathrm{r},2}\,. \\ \mathbf{L}_2 &= R_{\pi/3}\mathbf{L}_1 \end{aligned} \tag{2}$$

The second line of Eq. (2) leads to a Diophantine equation in the integers p, q, $\bar{p}$ and $\bar{q}$, and the set of angles which result in a commensurate supercell is given by[1–3]

$$\theta(p,q) = \cos^{-1}\left(\frac{p^2+4pq+q^2}{2(p^2+pq+q^2)}\right). \tag{3}$$

Consider an atom in the reference layer, with in-plane position $\mathbf{r}_0$. The corresponding atom in the twisted layer has position $\mathbf{r} = R_\theta \mathbf{r}_0$. The displacement due to twisting is $\delta(\mathbf{r}) = \mathbf{r} - \mathbf{r}_0 = \left(I - R_\theta^{-1}\right)\mathbf{r}$. If the layers form a commensurate supercell with lattice vectors $\mathbf{L}_i^{\mathrm{M}}$, say, the atoms will realign when the displacement is equal to a lattice vector, $\delta(\mathbf{L}_i^{\mathrm{M}}) = \mathbf{a}_{\mathrm{r},i}$:

$$\mathbf{L}_i^{\mathrm{M}} = \left(I - R_\theta^{-1}\right)^{-1} \cdot \mathbf{a}_i^1\,. \tag{4}$$

The cell spanned by $\mathbf{L}_i^{\mathrm{M}}$ is known as a moiré superlattice, and

$$L_{\mathrm{M}} \equiv \left|\mathbf{L}_i^{\mathrm{M}}\right| = \frac{a}{2\sin(\theta/2)}\,, \tag{5}$$

is known as the the moiré period, which is is not necessarily equal to the supercell period:

$$L_{\mathrm{sc}} = \frac{|p-q|\,a}{2\sin(\theta/2)} = |p-q|\,L_{\mathrm{M}}\,. \tag{6}$$

For $p \neq q$, there will be $(p-q)^2$ moiré periods in the supercell.

Having established a geometric description, we can model structural or electronic phenomena in a twisted bilayer using phenomenological or tight-binding models. These models can be paramaterized using first-principles calculations. However in practice this is difficult to do in real space because the size of and the number of atoms in the supercell becomes prohibitively large at smaller twist angles. Fortunately, we can take advantage of a useful mapping which allows us to parameterize systems at arbitrary twist angles using just a single cell of a commensurate bilayer.

The set of displacements of every atom in a moiré superlattice can be described by $\delta(\mathbf{r})$. Alternatively, we can describe the displacements by a set of local translations

$$\begin{aligned}\mathbf{s}(\mathbf{r}) &= \left(I - R^{-1}\right)\mathbf{r} \mod \{\mathbf{a}_{\mathrm{r},1}, \mathbf{a}_{\mathrm{r},2}\} \\ &\equiv A\cdot\mathbf{r}\end{aligned}\,, \tag{7}$$

i.e. at $\mathbf{r}$, the system is locally equivalent to an untwisted bilayer, with a relative in-plane slide $\mathbf{s}_\theta(\mathbf{r})$ between the layers, see Fig. 1. The set of translations $\mathbf{s}(\mathbf{r})$ is contained in a single primitive cell of the reference layer, even in the continuum limit. We call this space of translations configuration space[4–7]. This space can be traversed by taking an untwisted commensurate bilayer and sliding one layer over the other. Physical properties can be measured in configuration space, and we can use the inverse map,

$$\mathbf{r}(\mathbf{s}) = \left(I - R_\theta^{-1}\right)^{-1}\mathbf{s} = A^{-1}\mathbf{s}\,, \tag{8}$$

to parametrize a moiré superlattice in real space for arbitrary twist angles[7]. Derivatives in real space and configuration space are related by

$$\nabla_r = A^T\nabla_s\,, \tag{9}$$

which is useful for mapping quantities which depend on spatial derivatives, such as strains, to configuration space.

Stacking energy

It is well known layered systems interact via long-range van der Waals forces. For non-polar materials, this is facilitated by induced dipole−induced dipole, or London interactions, where fluctuations in the charge density of one layer lead to a dipolar response in the other layer, and vice versa. This can be described by a van der Waals potential in the layer separation d:

$$\mathcal{V}_{\mathrm{stack}}(d) = \frac{n}{m-n}\,|\mathcal{V}_0|\left[\left(\frac{d_0}{d}\right)^m - \frac{m}{n}\left(\frac{d_0}{d}\right)^n\right]\,, \tag{10}$$

where $\mathcal{V}_0$ is the depth of the potential well or cohesive energy *per unit cell*, d_0 is the equilibrium separation, and the indices (n,m) determine the curvature of the well about the minimum. Eq. (10) can be parametrized using first-principles calculations, which is done in Appendix B. For two slabs which extend infinitely in area, the energy is expected to behave like d^{-2} at larger separations, since the dipole-dipole interaction is integrated twice over an infinite area[8]. From first-principles calculations we found that this is not the case, and the long-range interactions in bilayer graphene and MoS_2 decay with $n \geq 6$. We suspect that this is because a bilayer is not adequately described as a pair of capacitor plates, but rather a single slab with a non-uniform charge density as in Fig. 1 (e). The non-zero overlap of states in the vacuum region may be screening the long-range interactions and could be responsible for larger than expected values of (n,m), although a more detailed study is required to verify this.

Electrostatic energy

The electrostatic energy of a dielectric slab in the presence of a perpendicular electric field $\mathcal{E}$ is

$$\mathcal{V}_{\mathrm{elec}}(P,\mathcal{E},d) = \Omega\left(\frac{1}{2\varepsilon_0\chi(d)}(P-P_0)^2 - \mathcal{E}P\right)\,, \tag{11}$$

where P and P_0 are the total and spontaneous polarization, respectively, A is the in-plane area of the bilayer, $\Omega = Ad$ is the volume of the bilayer, and $\chi(d)$ is the dielectric susceptibility, which in general depends on the geometry of the system. Eq. (11) assumes a linear response to the applied field, $P(\mathcal{E},d) = P_0 + \varepsilon_0\chi(d)\mathcal{E}$, which inserting into Eq. (11) gives:

$$\mathcal{V}_{\text{elec}}(\mathcal{E},d) = -\frac{1}{2}\varepsilon_0\alpha(d)\mathcal{E}^2 - \mathcal{E}p_0 \,, \tag{12}$$

where $\alpha = \Omega\chi$ is the polarizability, which describes the linear response of the dipole moment to the applied field, and $p_0 = \Omega P_0$ is the spontaneous dipole moment. When an electric field is applied, the layers are no longer non-polar, and the long-range interactions can no longer be considered induced dipole−induced dipole interactions. However, we can think of the interactions between the layers as arising due to fluctuations about a finite polarization, rather than zero polarization.

The effect of an applied field can be estimated from first-principles by measuring the stacking energy as a function layer separation for different field strengths. In Ref. 9, it was found that the electric field lowers the stacking energy of bilayer MoS_2 for large separations, leading to a breakdown of the bilayer at $\mathcal{E} \sim 2$ V Å^{-1}, although the precise behavior of the equilibrium layer separation as a function of applied field is unclear. In order to clarify this, we performed detailed first-principles calculations in Appendix B. In Fig. 5 (a) we plot the potential energy curves for bilayer MoS_2 as a function of d for different values of applied field. We see that the electric field lowers the energy at larger separations, and the bilayer becomes unstable at $\mathcal{E}_{\text{crit}} \approx 2.25$ V Å^{-1}, similar to the results obtained in Ref. 9. By calculating the Mülliken charges on each layer in Fig. 5 (b), we find that there is an interlayer charge transfer when an electric field is applied. The charge transfer is linear in $\mathcal{E}$ above $\mathcal{E} \approx 0.27$ V Å^{-1}, below which little or no charge transfer is observed. We attribute this to internal field effects, similar to the depolarizing field observed in ferroelectric thin films. see Fig. 1 (d). The internal field could be accounted for in the electrostatic energy as[9] $\mathcal{V}_{\text{int}} = -\frac{1}{2}\mathcal{E}_{\text{int}}P$. In the interest of simplicity, we neglect internal field effects in our model.

In Fig. 6 (a) we plot the dipole moment $p(\mathcal{E})$ for several values of d. For field strengths strong enough to overcome internal field effects, the dipole moment is linear in $\mathcal{E}$, but also in d. Thus, as shown in Fig. 6 (b), the polarizability is approximately linear in d,

$$\alpha(d) = \alpha_0 + \alpha_1\left(\frac{d}{d_0} - 1\right) \,, \tag{13}$$

where α_0 and α_1 are both positive and have units of Å^3. Taking $(n,m) = (n,2n)$, we can write the energy, exlcuding elastic contributions, as

$$\begin{aligned}\mathcal{V}_{\text{tot}}(d,\mathcal{E}) = |\mathcal{V}_0|&\left[\left(\frac{d_0}{d}\right)^{2n} - 2\left(\frac{d_0}{d}\right)^{n}\right] \\ &- \mathcal{E}p_0 - \frac{1}{2}\varepsilon_0\left(\alpha_0 + \alpha_1\left(\frac{d}{d_0} - 1\right)\right)\mathcal{E}^2\end{aligned} \,. \tag{14}$$

By plotting contours of the energy as a function of d for fixed values of $\mathcal{E}$, see Fig. 2 (a), we can see that the stacking energy is lowered by the electric field, consistent with results from first-principles calculations. At zero field, $\mathcal{V}_{\text{stack}}$ has a minimum at the equilibrium separation $d_{\text{min}} = d_0$, and a maximum (for $d > d_{\text{min}}$) at $d_{\text{max}} \to \infty$. When a field is applied, $\mathcal{V}_{\text{stack}}$ diverges as $d \to \infty$. This makes physical sense: increasing d will increase the total dipole moment and lower the total energy. For a non-zero field, d_{max} has a finite value, at the top of the energy barrier which separates d_{min} and $d \to \infty$. As the field strength increases, d_{min} and d_{max} move closer together, eventually meeting at a critical point $(d_{\text{crit}}, \mathcal{E}_{\text{crit}})$ where the energy barrier vanishes, and the bilayer becomes unstable,

$$\begin{aligned} d'_{\text{crit}} &= \left(\frac{2n+1}{n+1}\right)^{\frac{1}{n}} \\ \mathcal{E}'_{\text{crit}} &= 2n\sqrt{\frac{(n+1)^{1+\frac{1}{n}}}{(2n+1)^{2+\frac{1}{n}}}} \end{aligned} \,, \tag{15}$$

where $d' \equiv \frac{d}{d_0}$ and $\mathcal{E}' \equiv \sqrt{\frac{\varepsilon_0\alpha_1 d_0}{|\mathcal{V}_0|}}\mathcal{E}$. In Fig. 2 (b) we show d_{min} and d_{max} as a function of $\mathcal{E}$ for several values of n. The solid red line shows Eq. (15), which separates d_{min} and d_{max}. Interestingly, the behavior is highly sensitive to the value of n. For larger values of n, which are predicted from first-principles calculations, d_{min} does not change by much until $\mathcal{E} \sim \mathcal{E}_{\text{crit}}$, where it increases by about 10% before the bilayer becomes unstable. For smaller values of n, the layers separate more easily because the potential well is shallower, but the breakdown occurs at smaller field strengths.

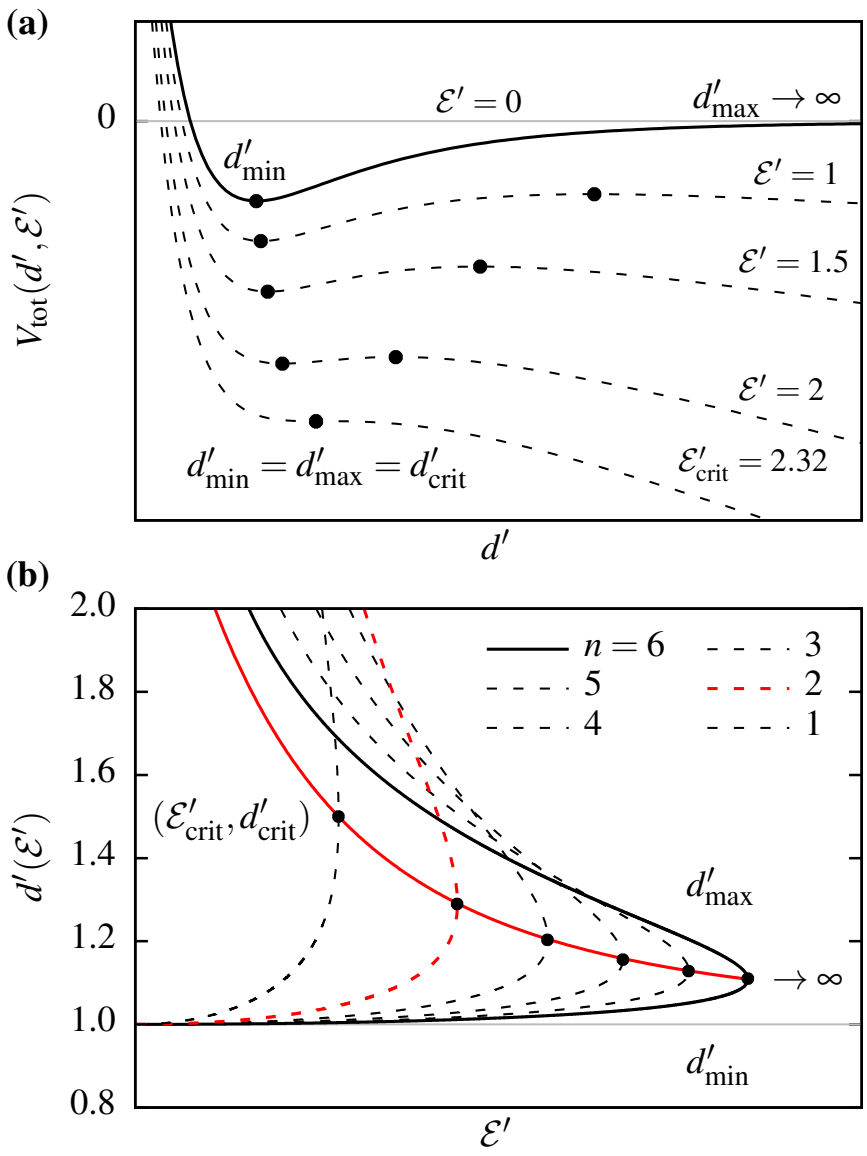

SUPPLEMENTARY FIG 2: Analytic results from Eq. (14). **(a)**: Total energy from Eq. (14) as a function of d for increasing values of $\mathcal{E}$. The points show the positions of $d_{\min}$ and $d_{\max}$ on each curve. The lowest curve is for field strength of $\mathcal{E} = \mathcal{E}_{\crit}$, where $d_{\min} = d_{\max} \equiv d_{\crit}$. **(b)**: $d_{\min}$ and $d_{\max}$ as a function of $\mathcal{E}$ for different values of n, increasing from left to right. The solid black curve is $n = 6$, and the dashed red curve is the theoretical value $n = 2$. The solid red curve shows the critical values $(d_{\crit}, \mathcal{E}_{\crit})$ from Eq. (15). The critical points on each curve are marked, i.e. when $d = d_{\crit}$ and the bilayer breaks down.

Elastic energy

The elastic energy in Eq. 2 is given as a contraction of the strain tensors with the fourth rank elasticity tensor[7,10]:

$$C_{11} = \begin{bmatrix} B+\mu & 0 \\ 0 & B-\mu \end{bmatrix}, \quad C_{12} = \begin{bmatrix} 0 & \mu \\ \mu & 0 \end{bmatrix}, \\ C_{21} = \begin{bmatrix} 0 & \mu \\ \mu & 0 \end{bmatrix}, \quad C_{22} = \begin{bmatrix} B-\mu & 0 \\ 0 & B+\mu \end{bmatrix} \tag{16}$$

and is given explicitly as

$$\begin{aligned}\mathcal{V}_{\text{elastic}} &= \frac{1}{2}\left[B\left(\varepsilon_{11}+\varepsilon_{22}\right)^2+\mu\left(\left(\varepsilon_{11}-\varepsilon_{22}\right)^2+\left(\varepsilon_{12}+\varepsilon_{21}\right)^2\right)\right] \\ &= \frac{1}{2}\left[B\left(\partial_x U_x+\partial_y U_y\right)^2+\mu\left(\left(\partial_x U_x-\partial_y U_y\right)^2+\left(\partial_x U_y+\partial_y U_x\right)^2\right)\right]\end{aligned} \tag{17}$$

The strain tensor in configuration space is[7]

$$\varepsilon_{ij} = \frac{1}{2}\left((\partial_i u_k)A_{kj}+(\partial_j u_k)A_{ki}\right) \tag{18}$$

which allows us to write down the elastic energy in configuration space:

$$\mathcal{V}_{\text{elastic}} = \frac{\theta^2}{2}\left[B\left(\partial_{s_x}u_{s_y}-\partial_{s_y}u_{s_x}\right)^2+\mu\left(\left(\partial_{s_x}u_{s_y}+\partial_{s_y}u_{s_x}\right)^2+\left(\partial_{s_x}u_{s_x}-\partial_{s_x}u_{s_x}\right)^2\right)\right] \tag{19}$$

It is convenient to work in terms of the lattice vectors $\mathbf{a}_{\text{r},1}$ and $\mathbf{a}_{\text{r},2}$. Under this transformation, the displacement transforms as $\mathbf{u} \to g\mathbf{u}$ and the strain tensor transforms as $\varepsilon_{ij} \to g^{-1}_{i\alpha}\varepsilon_{\alpha\beta}g_{\beta j}$, where $g = \begin{bmatrix}1 & 1/2 \\ 0 & \sqrt{3}/2\end{bmatrix}$. The elastic energy is then

$$\mathcal{V}_{\text{elastic}} = \frac{\theta^2}{2}\left[B\left(\partial_{a_x}u_{a_y}-\partial_{a_y}u_{a_x}\right)^2+\mu\left(\frac{4}{3}\left(\partial_{a_x}u_{a_y}+\partial_{a_y}u_{a_x}\right)^2+\left(\partial_{a_x}u_{a_x}-\partial_{a_y}u_{a_y}\right)^2\right)\right] \tag{20}$$

SUPPLEMENTARY NOTE 2: FIRST-PRINCIPLES CALCULATIONS

Because functionals within the generalized gradient approximation (GGA) tend to underestimate the cohesive energy of van der Waals systems, the different VDW-corrected functionals in SIESTA were tested by measuring the stacking energy of bilayer graphene as a function of layer separation, see Fig. 3. The rest of the calculations were performed using the C09 functional, as it was found to give good results for both bilayer graphene and MoS_2.

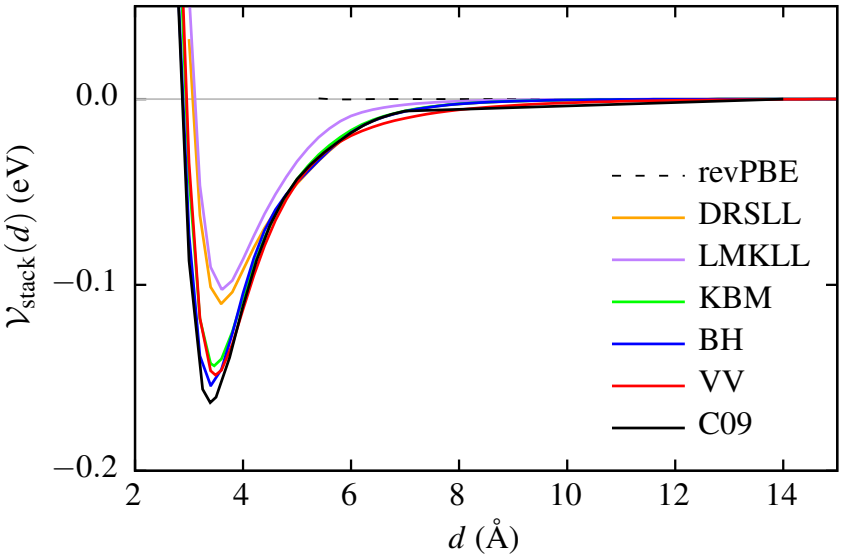

SUPPLEMENTARY FIG 3: Stacking energy as a function of layer separation for bilayer graphene for various VDW-corrected functionals in SIESTA[11]: revPBE[12] (GGA), DRSLL (DF1)[13,14], LMKLL (DF2)[13,15], KMB[13,16], C09[13,17], BH[13,18], VV[19].

Parametrizing the stacking energy

We can parameterize the stacking energy by calculating $\mathcal{V}_0$, d_0 and the two indices (n,m). Using suitable values for (n,m), a fit to the stacking energy as a function of layer separation was obtained using Eq. (10), which is shown in Fig. 4 for bilayer graphene and MoS_2 with 3R stacking. The parameters used to fit Eq. (10) to the first-principles calculations are given in Table I.

Material	a (Å)	$\mathcal{V}_0$ (eV)	d_0 (Å)	(n,m)
graphene	2.473	-0.163	3.393	$(6,8)$
MoS_2 (3R)	3.164	-0.165	6.716	$(8,15)$

SUPPLEMENTARY TABLE I: Parameterization of $\mathcal{V}_{\text{stack}}(d)$ for bilayer graphene and MoS_2 from first-principles calculations.

Parametrizing the electrostatic energy

To parametrize $\mathcal{V}_{\text{elec}}$, an electric field was applied in the out-of-plane direction. A dipole correction[20–23] was used in the vacuum region to prevent long-range interactions between periodic images. The resulting dipole moment in the out-of-plane direction was then measured.

We first performed geometry relaxations of bilayer MoS_2 for electric fields of increasing strength. We found that the layer separation increases only marginally (a very low force tolerance is required to see this, otherwise the layers do not move) until around $\mathcal{E} \sim 2$ V Å^{-1}, where the layers begin to separate and the bilayer quickly becomes unstable. In order to investigate this peculiar behaviour, we calculated the stacking energy curves for various electric field strengths, see Fig. 5 (a). We can see that

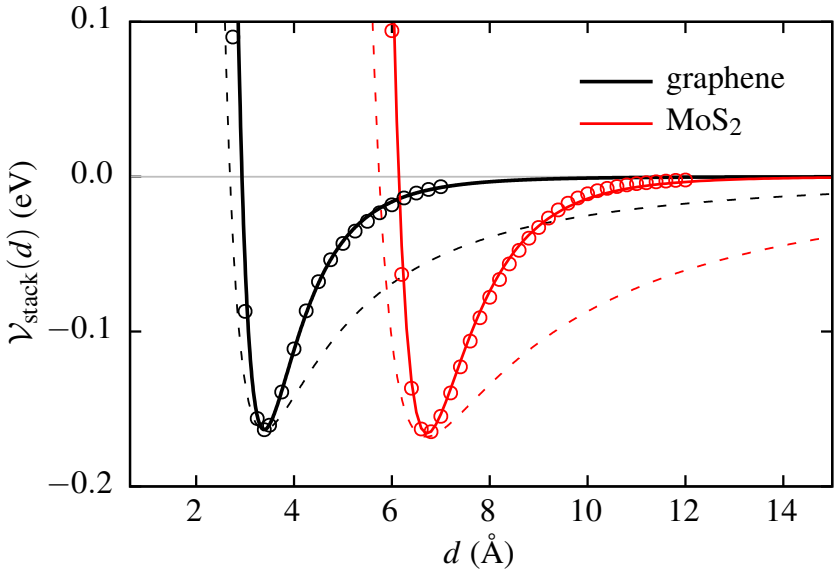

SUPPLEMENTARY FIG 4: Parameterization of $\mathcal{V}_{\text{stack}}(d)$ for bilayer graphene and MoS_2 (3R stacking). The points show results from DFT calculations, and the solid lines show the parameterization using the values in Table I. The dashed lines show the same parameterization, but with the smaller index changed to 2.

the electric field lowers the stacking energy, in agreement with our model. In Fig. 5 (b) we show the Mülliken chares as forces on each layer as a function of electric field, which indicates that there is a transfer of charge across the layers as an electric field is applied, verifying similar results obtained in Ref. 9.

For each value of d, we calculate the dipole moment as a function of electric field, $p(\mathcal{E})$, as shown in Fig. 6 (a). We see that, at smaller values electric field strength, $\mathcal{E} < 0.27$ V Å^{-1}, changing the distance has little effect on the polarizability α. As mentioned previously, we attribute this to internal field effects. In order to neglect these effects, we measure the polarizability $\alpha(d)$ at field strengths which are large enough to overcome the internal fields. At stronger values of field $\alpha(d)$ increases linearly with d, see Fig. 6 (b).

Parameterization in configuration space

Calculations were repeated to parameterize $\mathcal{V}_0$, d_0, α_0 and α_1 as a function of $\mathbf{s}$. The high symmetry stacking configurations AA (metal over metal), AB/BA (metal over chalcogen), and the saddle point (SP) all lie along the configuration space diagonal. Thus, it was sufficient to perform a series of calculations along the diagonal, and use a 2D Fourier interpolation to parameterize the model everywhere in configuration space. One layer was fixed, and the other layer was translated by $\mathbf{s} = s(\mathbf{a}_1 + \mathbf{a}_2)$, $s \in [0,1]$, and the aforementioned quantities were measured on a fine grid of values of s. The interpolation was done following similar approaches in previous studies[7,24–26]: each quantity is written as a Fourier expansion. The results from the first-principles calculations at different values of $\mathbf{s}$ are used to fit the Fourier coefficients, and a smooth interpolation of each quantity is obtained everywhere in configuration space. The reciprocal lattice vectors $\mathbf{G}$ of the same length are sorted into shells, and the first few shells are sufficient to obtain good parameterizations. The first-principles results and parameterization using the first three shells are shown in Fig. 4 for 3R and 2H stacked bilayer MoS_2.

After parameterizing the model, we can examine the effect of an electric field on the system in configuration space. Fig. 7 (a) shows the layer separation in configuration space at different electric field values for 3R MoS_2. Without lattice relaxation, only the quadratic electrostatic term affects the layer separation. We can see that the layer separation increases non-uniformly in configuration space, leading to a corresponding reduction in stacking energy, shown in Fig. 7 (b). We only show up to $\mathcal{E} = 1.68$ V Å^{-1} because that is the smallest critical field at which $d_{\text{min}} \to \infty$ somewhere in configuration space. We examine this in more detail in Fig. 7 (c) by showing d_{min} as a function of electric field at the AA, AB and SP points. We can see that the critical field values for the AB and SP points are considerably larger. We could reach stronger field strengths by including terms proportional to ∇d in the elastic energy from von Karman plate theory[24], but this would make the model considerably more difficult to solve, requiring either solutions to fourth order differential equations or a more difficult optimization problem. After lattice relaxation, the AA regions shrink considerably, and the critical fields of interest for the domain wall are $\mathcal{E}^{\text{SP}}_{\text{crit}}$ and $\mathcal{E}^{\text{AB}}_{\text{crit}}$,

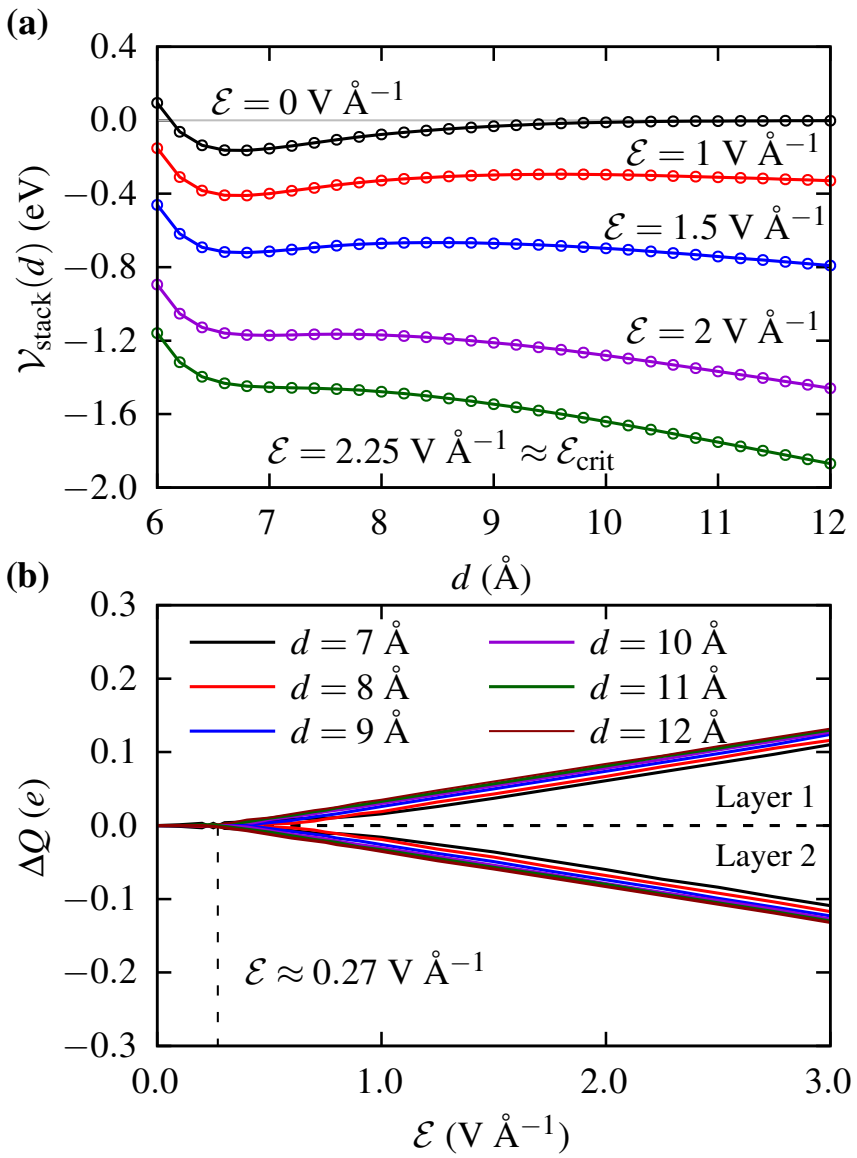

SUPPLEMENTARY FIG 5: Stacking energy and Mülliken charges on each layer as a function of d and $\mathcal{E}$. **(a)**: $\mathcal{V}_{\text{stack}}(d)$ for different fixed values of electric field. **(b)**: Change in Mülliken charges ΔQ of each layer as a function of electric field. The vertical dashed line indicates the field strength beyond which internal field effects are mitigated.

since the domain wall is across the path AB $\rightarrow$ SP $\rightarrow$ BA. However, without including nonlinear terms in the elastic energy, we are limited by the smallest critical field, $\mathcal{E}_{\text{crit}}^{\text{AA}}$.

In Fig. 8 (a) we show the spontaneous polarization $P_0(s)$ along the diagonal in configuration space. The coupling between the polarization and the field leads to an even splitting of the AB and BA wells, increasing one and decreasing the other, which is shown in Fig. 8 (b).

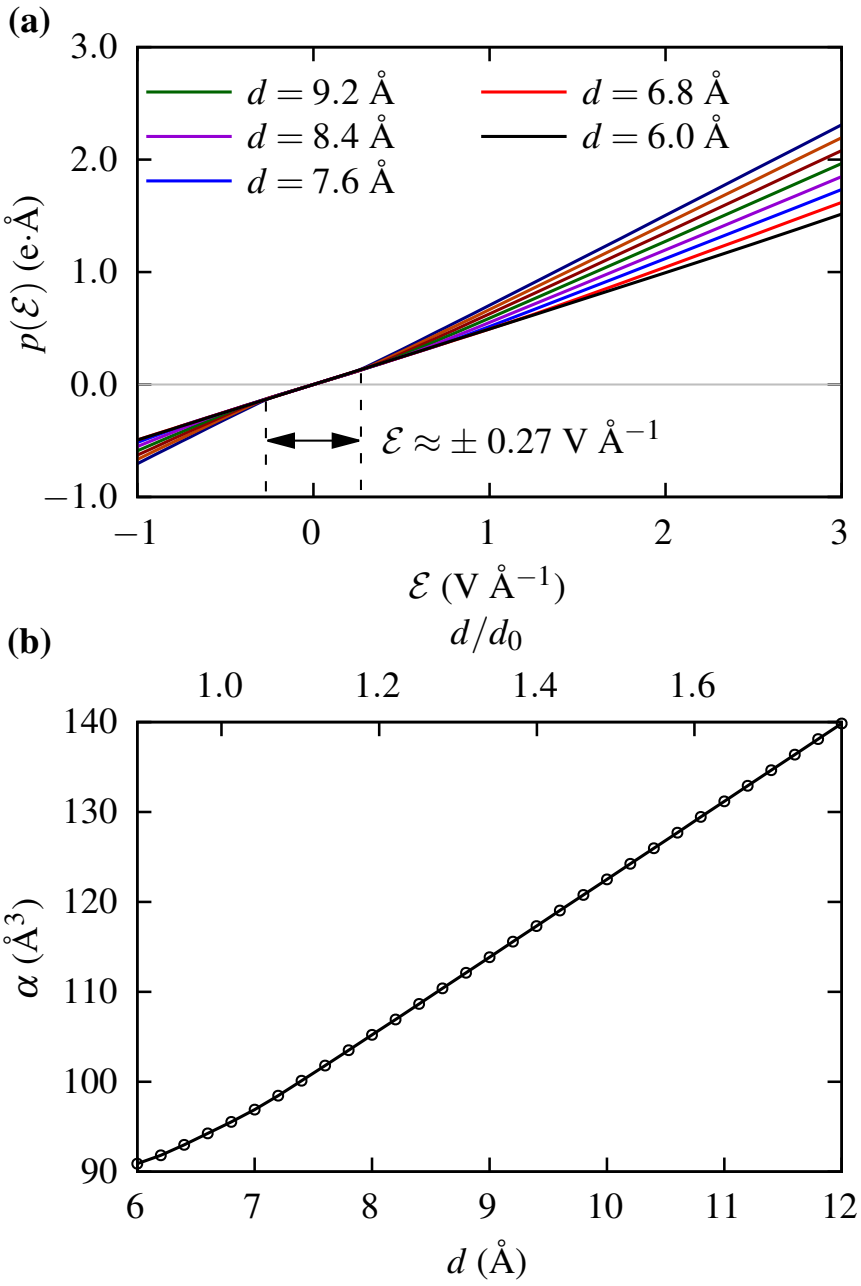

SUPPLEMENTARY FIG 6: Out-of-plane dipole moment and polarizability as a function of d and $\mathcal{E}$. **(a)**: Out-of-plane dipole moment $p(\mathcal{E})$ for various fixed values of d. The range of field values for which internal field effects are significant is indicated by the dashed lines. **(b)**: Polarizability $\alpha(d)$, measured at $\mathcal{E} > 0.27$ V Å^{-1} in order to neglect internal field effects.

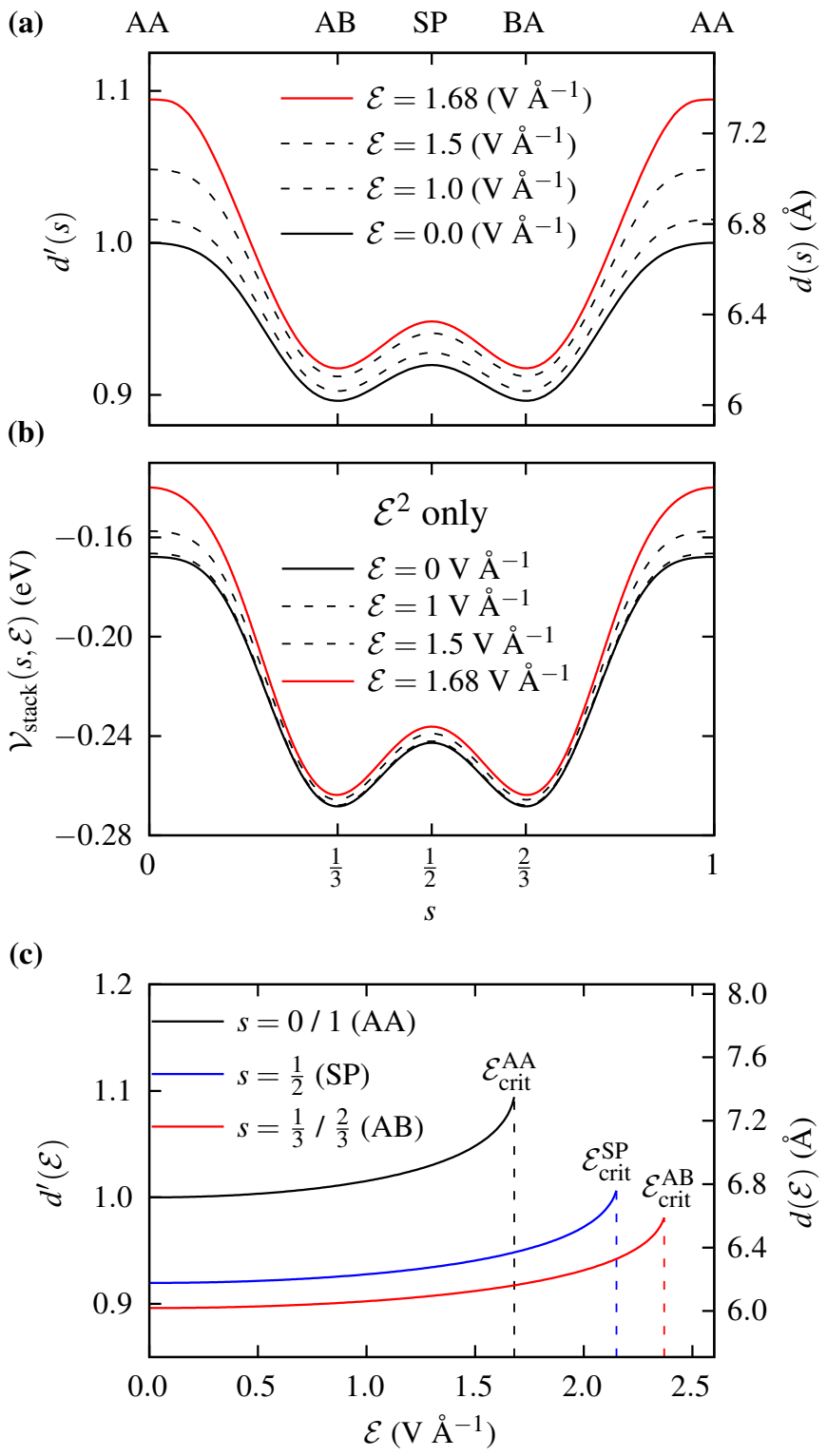

SUPPLEMENTARY FIG 7: Effect of the quadratic electrostatic term on the layer separation and stacking energy in configuration space. **(a)**: Layer separation along the configuration space diagonal for different values of $\mathcal{E}$ for 3R MoS_2. **(b)**: Stacking energy along the diagonal in configuration space at different field strengths, including only the quadratic electrostatic term. **(c)**: Layer separation as a function of $\mathcal{E}$ for the AA, SP and AB stacking configurations. The stacking configurations have critical field values $\mathcal{E}^{\text{AA}}_{\text{crit}} = 1.68$ V Å^{-1}, $\mathcal{E}^{\text{SP}}_{\text{crit}} = 2.15$ V Å^{-1} and $\mathcal{E}^{\text{AB}}_{\text{crit}} = 2.37$ V Å^{-1}, respectively.

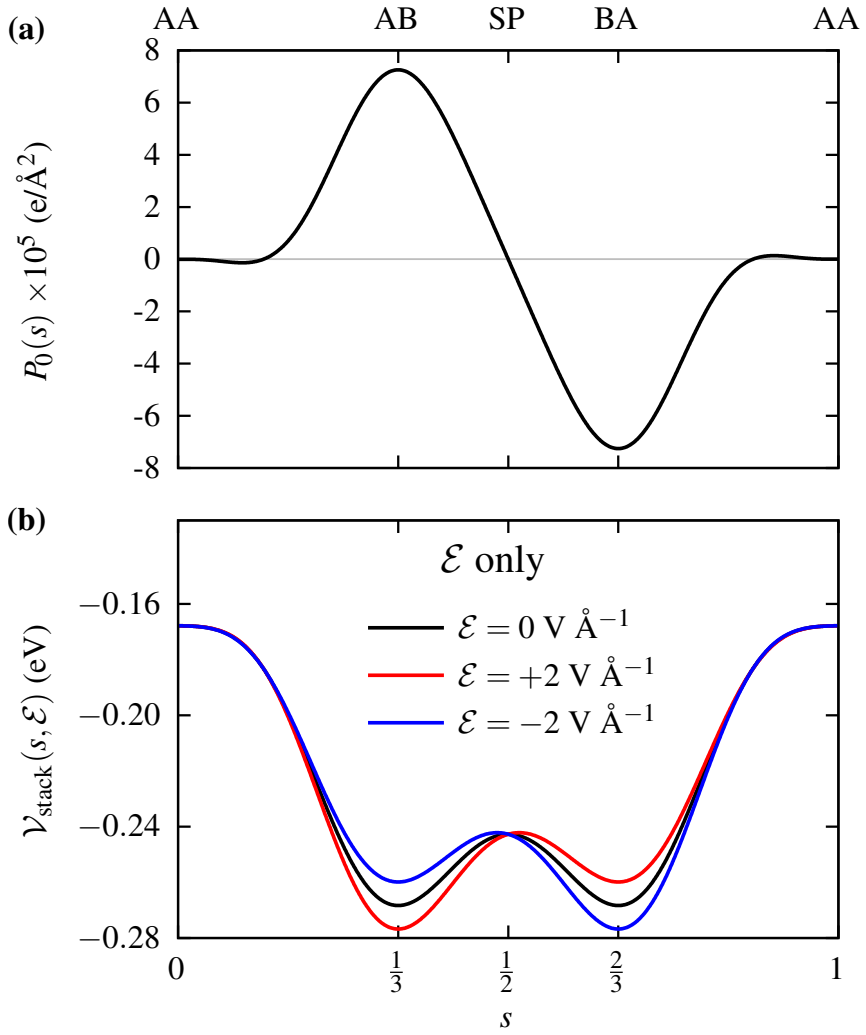

SUPPLEMENTARY FIG 8: Spontaneous polarization and its effect on the stacking energy in configuration space for 3R MoS_2. **(a)**: Spontaneous polarization P_0 along the diagonal through configuration space for 3R MoS_2. **(b)**: Stacking energy along the diagonal in configuration space at different field strengths, including only the linear electrostatic term.

SUPPLEMENTARY NOTE 4: FRENKEL-KONTOROVA MODEL

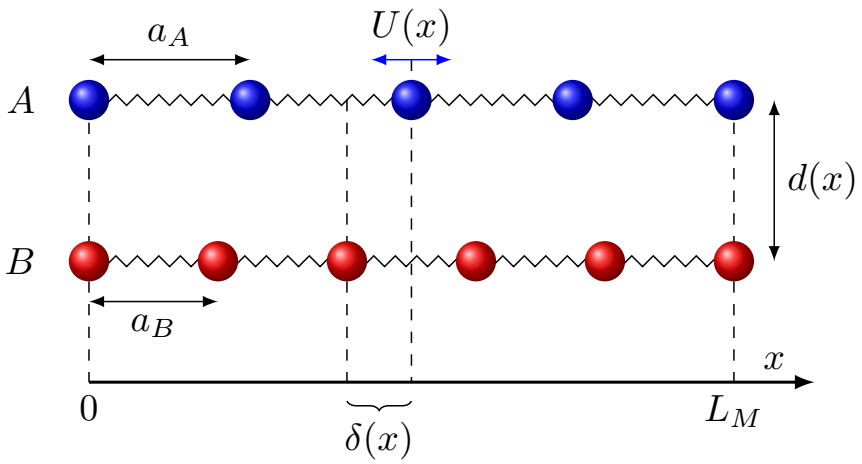

SUPPLEMENTARY FIG 9: Sketch of a 1D FK model. The layers are represented by chains of atoms A and B, connected by springs. The supercell period of the chains L_{M} is shown along the x-axis. The lattice mismatch plays the role of the twist angle.

The Frenkel-Kontorova (FK) model was first introduced in the 1930s and is widely used in condensed matter physics[27,28]. It is a discrete model where a chain of atoms is subject to a rigid periodic potential, from a substrate for example[27,29–31]. The FK model has been used as a 1D representation of twisted bilayer systems[5,25,32], replacing the rigid substrate with a second chain of atoms which can also deform, see Fig. 9, and has been used to describe commensurate-incommensurate phase transitions[32,33], lattice relaxation and domain structures[7,25,34].

Because the dielectric response does not break any symmetries, we study its effect on the domain walls using a 1D FK model. For 3R MoS_2, the domain walls are along the path AB $\rightarrow$ SP $\rightarrow$ BA, so we use those points to parameterize the stacking energy[32,33,35] in a one dimensional version of configuration space,

$$\begin{aligned} \mathcal{V}_0^{\mathrm{FK}}(s) &= \mathcal{V}_0^{+} + \mathcal{V}_0^{-}\cos(2\pi s) \\ \mathcal{V}_0^{\pm} &= \frac{1}{2}\left(\mathcal{V}_0\left(\tfrac{1}{2}\right) \pm \mathcal{V}_0\left(\tfrac{1}{3}\right)\right) \end{aligned}, \tag{21}$$

described by a single variable s, the relative displacement between the atoms in the two chains, and similarly for d_0, α_0 and α_1.

The total energy in configuration space is

$$V_{\mathrm{tot}}^{\mathrm{FK}} = \frac{1}{A_{\mathrm{s}}}\int_{A_{\mathrm{s}}}\left[\frac{1}{2}B\theta^2\left(\partial_s u\right)^2 + \mathcal{V}_{\mathrm{stack}}^{\mathrm{FK}}(s+u(s),d) + \mathcal{V}_{\mathrm{elec}}^{\mathrm{FK}}(s+u(s),d,\mathcal{E})\right]\mathrm{d}s\,, \tag{22}$$

where θ is the lattice mismatch, B is the bulk modulus of MoS_2[7] and $\mathcal{V}_{\mathrm{stack}}$ and $\mathcal{V}_{\mathrm{elec}}$ include the displacement $u(s)$ to allow for relaxations. Eq. 22 can be also be minimized using optimization techniques, but in 1D the differential equations are easy enough to solve. Minimizing with respect to both u and d, we get

$$\begin{aligned} \partial_u\left[\mathcal{V}_{\mathrm{stack}}^{\mathrm{FK}}(s+u(s),d) + \mathcal{V}_{\mathrm{elec}}^{\mathrm{FK}}(s+u(s),d,\mathcal{E})\right] - B\theta^2\partial_s^2 u(s) = 0 \\ \partial_d\left[\mathcal{V}_{\mathrm{stack}}^{\mathrm{FK}}(s+u(s),d) + V_{\mathrm{elec}}^{\mathrm{FK}}(s+u(s),d,\mathcal{E})\right] = 0 \end{aligned}. \tag{23}$$

The second equation can be solved independently to obtain $d_{\mathrm{min}}(s,\mathcal{E})$. This is inserted into the first equation, which can be solved numerically.

In Fig. 10 we show results for various values of θ at zero field. For larger θ, the atoms do not move much from their initial stacking configuration. As θ decreases, the elastic energy is reduced, and the atoms relax more. We see from Fig. 10 (a), the total displacement $s+u(s)$, that the atoms move to maximize the area around $s=\frac{1}{2}$, the stacking configuration with lowest energy. Figs. 10 (c) and (d) show the effect of the lattice relaxation on the stacking energy and layer separation. We can see that a domain structure forms, with wide AB/BA regions and narrow SP regions. The two are separated by a domain wall, the width

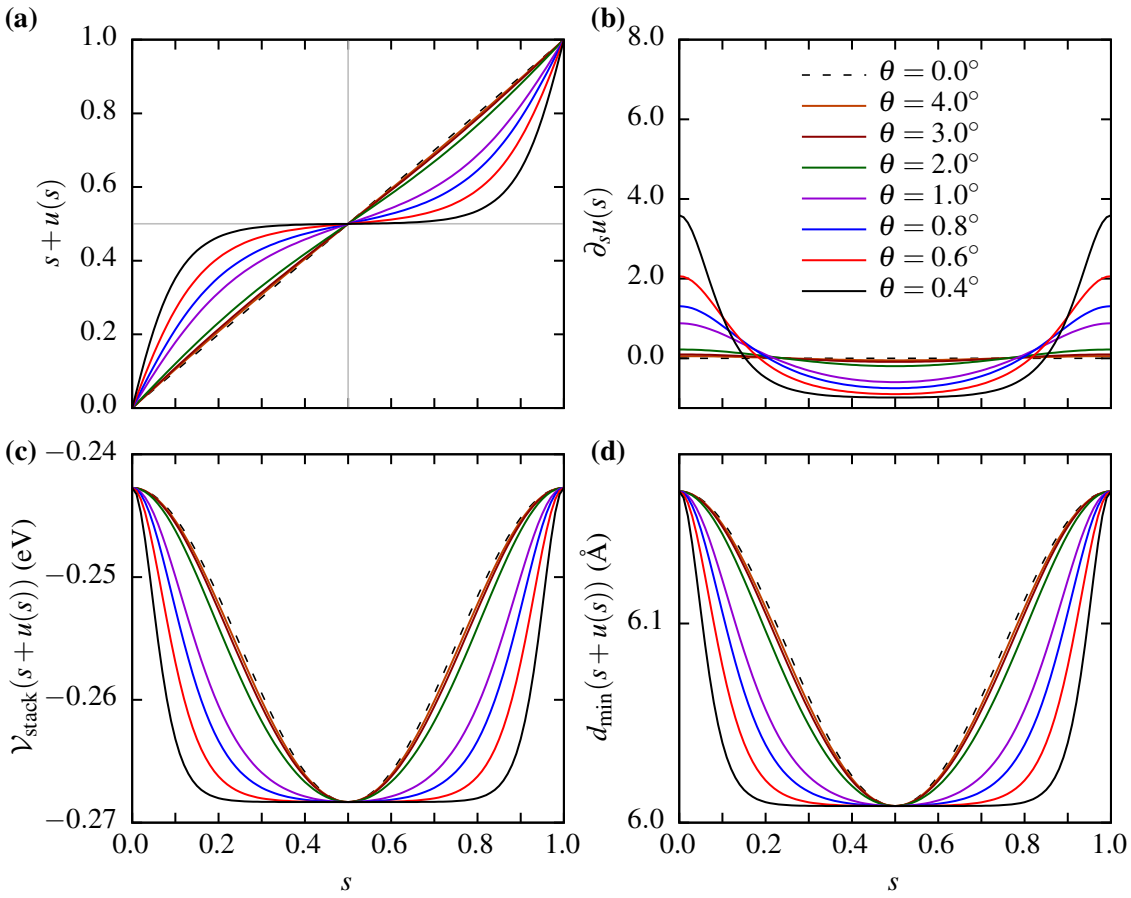

SUPPLEMENTARY FIG 10: Solutions to Eq. (23) at zero field for various twist angles: **(a)**: total displacement in configuration space $s+u(s)$, **(b)**: change in displacement $\partial_s u(s)$, equivalent to the strain tesnor in 1D, **(c)**: stacking potential as a function of total displacement $V_{\text{stack}}(s+u(s))$ and **(d)**: equilibrium layer separation as a function of total displacement $d_{\text{min}}(s+u(s))$.

of which is proportional to θ. Fig. 10 (b) shows the change in displacement $\partial_s u(s)$, which is proportional to the strain tensor in 1D, from which we see that there is a large strain gradient across the domain wall.

At $s=0$, we have the analytic approximation[32]:

$$u(s) = \frac{2}{\pi}\tan^{-1}\left(e^{2\pi\sqrt{\frac{V_0^- - \frac{1}{2}\varepsilon_0\mathcal{E}^2\alpha_0^-}{B\theta^2}}s}\right) - \frac{1}{2}\,, \tag{24}$$

which is shown alongside the numerical solutions to Eq. (23) in Fig. 11 (a). We can approximate the width of the domain wall as

$$w \sim \frac{1}{2}\sqrt{\frac{B\theta^2}{\left(V_0^- - \frac{1}{2}\varepsilon_0\mathcal{E}^2\alpha_0^-\right)}} \tag{25}$$

illustrating the dependence on both twist angle and electric field. In Fig. 11 (b) we plot $w(\mathcal{E})$ for several values of θ. w diverges at a critical field $\mathcal{E}^w_{\text{crit}} = \sqrt{\frac{2V_0^-}{\varepsilon_0\alpha_0^-}}$ which is independent of the lattice mismatch. For MoS_2, we have $\mathcal{E}^w_{\text{crit}} \approx 2.47$ V Å^{-1} which is larger than the largest critical field $\mathcal{E}^{\text{AB}}_{\text{crit}} = 2.37$ V Å^{-1}.

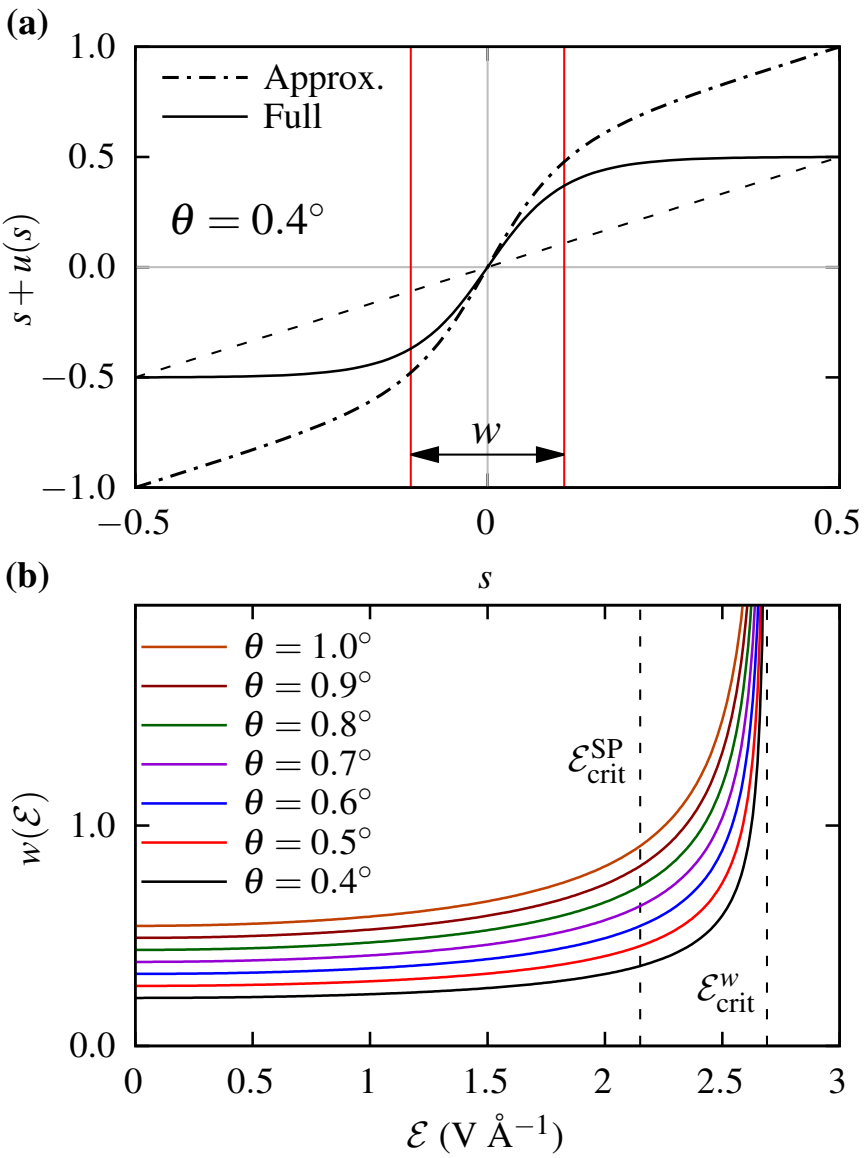

SUPPLEMENTARY FIG 11: Analysis of the domain wall width from the 1D FK model. **(a)**: Displacement $u(s)$ obtained by solving Eq. (23) numerically and from the analytic approximation Eq. (24) about $s = 0$. The domain width Eq. (25) is indicated by the vertical red lines. **(b)**: $w(\mathcal{E})$ for various lattice mismatches from Eq. (25). The dashed lines indicate the minimum critical field in the FK model, $\mathcal{E}^{\mathrm{SP}}_{\mathrm{crit}} = 2.15$ V Å^{-1} and the critical field at which the domain width diverges, $\mathcal{E}^{w}_{\mathrm{crit}} \approx 2.47$ V Å^{-1}.

SUPPLEMENTARY NOTE 4: ADDITIONAL DATA ON TWIST ANGLE AND ELECTRIC FIELD DEPENDENCE OF STACKING DOMAINS

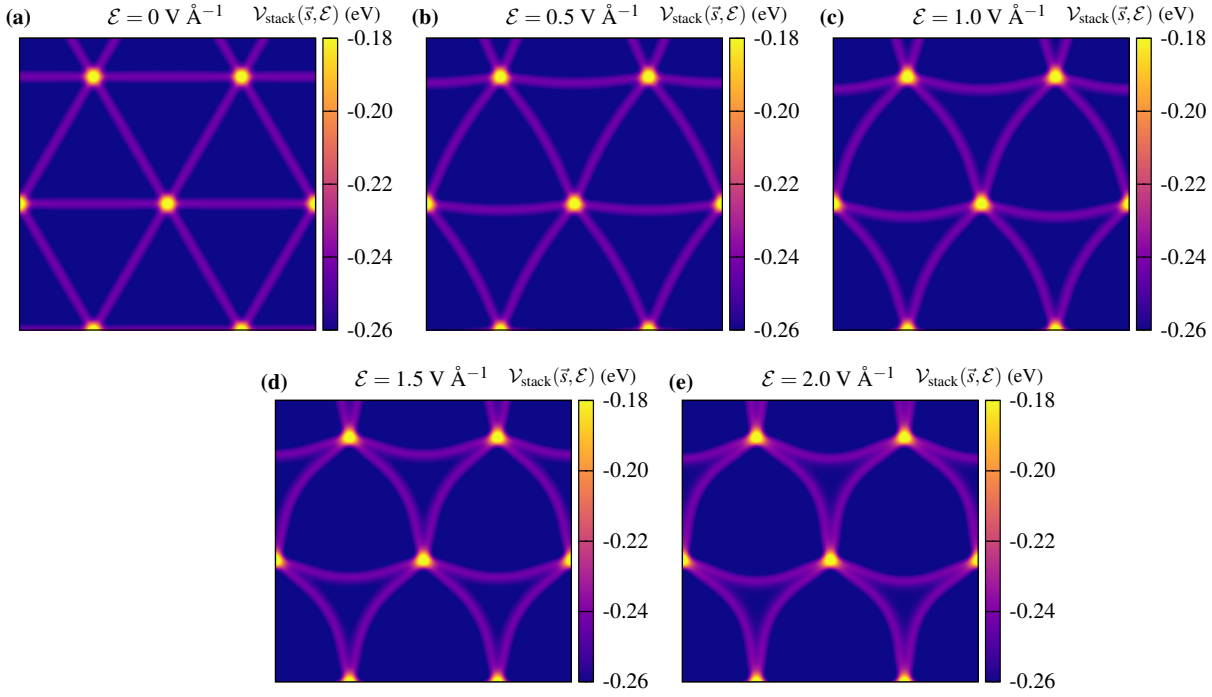

SUPPLEMENTARY FIG 12: Lattice relaxtion for 3R stacked bilayer MoS_2 at a twist angle of $\theta = 0.4^\circ$ for several electric field values.

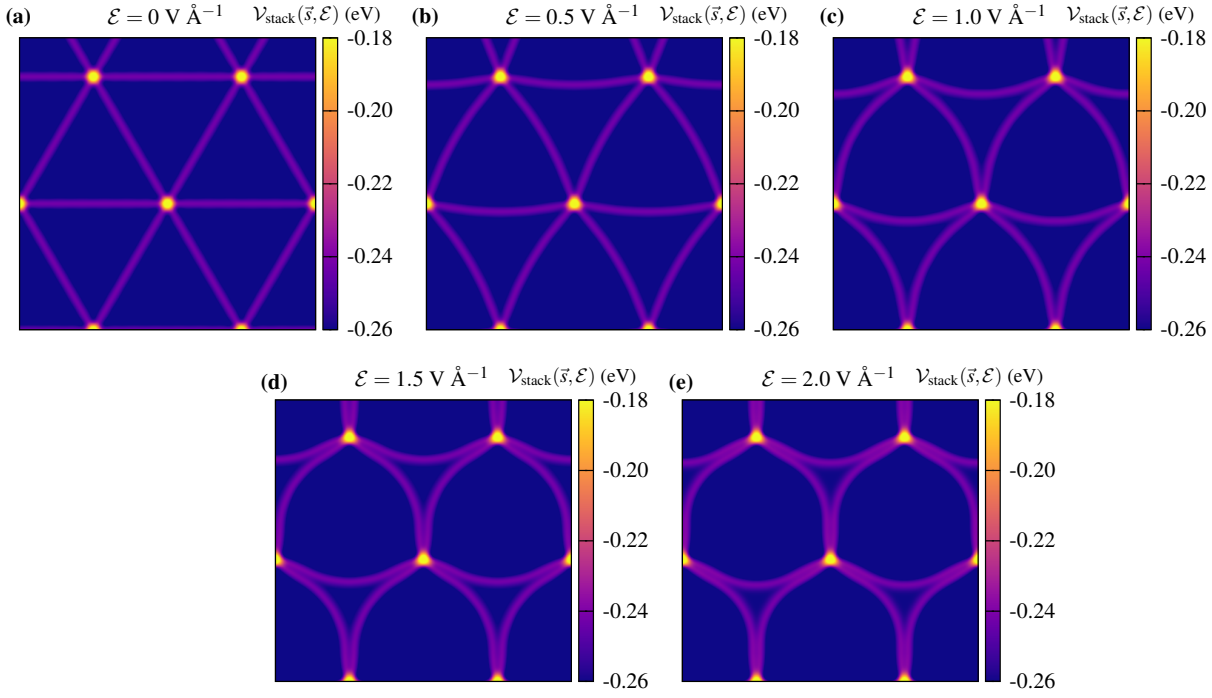

SUPPLEMENTARY FIG 13: Lattice relaxtion for 3R stacked bilayer MoS_2 at a twist angle of $\theta = 0.3^\circ$ for several electric field values.

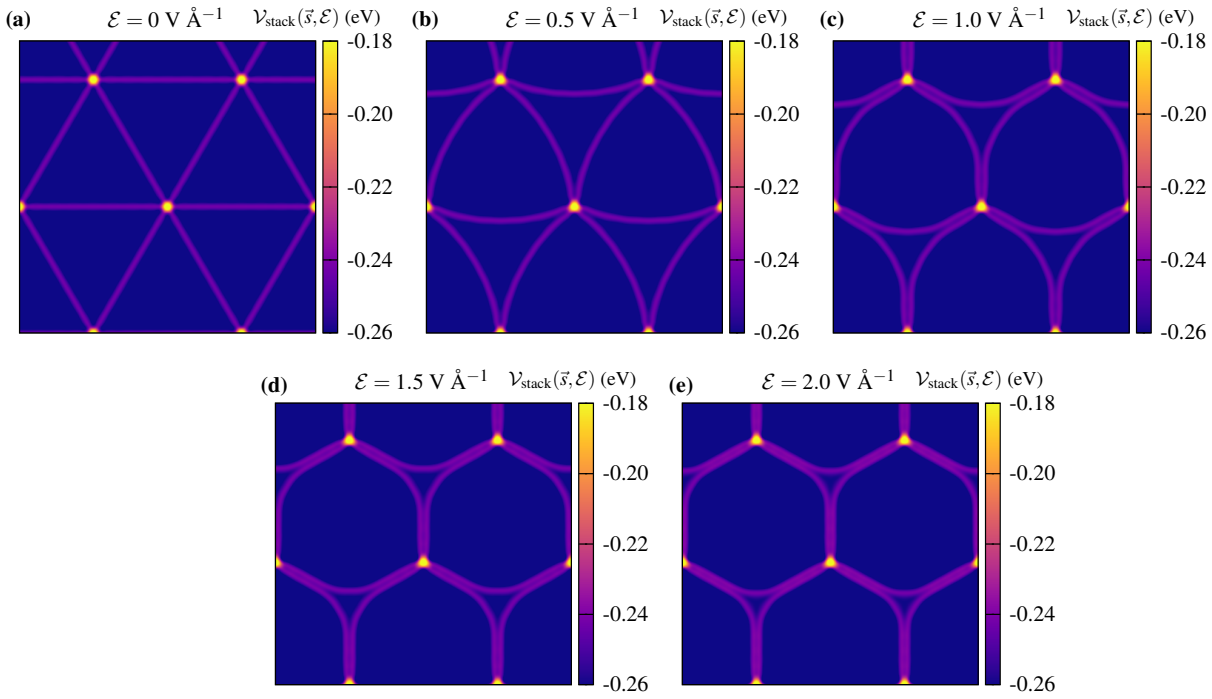

SUPPLEMENTARY FIG 14: Lattice relaxtion for 3R stacked bilayer MoS_2 at a twist angle of $\theta = 0.2^\circ$ for several electric field values.

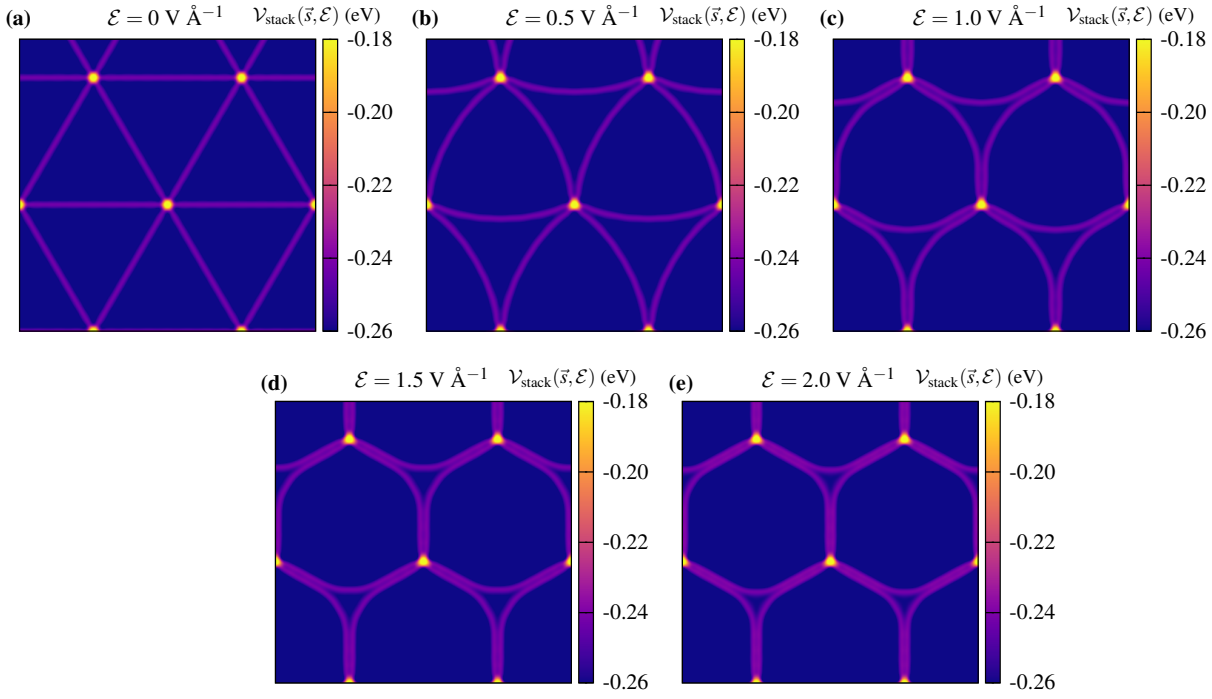

SUPPLEMENTARY FIG 15: Lattice relaxtion for 3R stacked bilayer MoS_2 at a twist angle of $\theta = 0.1^\circ$ for several electric field values.

[1] S. Shallcross, S. Sharma, E. Kandelaki, and O. Pankratov, Phys. Rev. B **81**, 165105 (2010).
[2] E. J. Mele, Phys. Rev. B **81**, 161405 (2010).
[3] K. Hermann, Journal of Physics: Condensed Matter **24**, 314210 (2012).
[4] S. Carr, D. Massatt, S. Fang, P. Cazeaux, M. Luskin, and E. Kaxiras, Phys. Rev. B **95**, 075420 (2017).
[5] P. Cazeaux, M. Luskin, and E. B. Tadmor, Multiscale Modeling & Simulation **15**, 56 (2017).
[6] D. Massatt, M. Luskin, and C. Ortner, Multiscale Modeling & Simulation **15**, 476 (2017).
[7] S. Carr, D. Massatt, S. B. Torrisi, P. Cazeaux, M. Luskin, and E. Kaxiras, Phys. Rev. B **98**, 224102 (2018).
[8] R. Tadmor, Journal of physics: Condensed matter **13**, L195 (2001).
[9] E. J. Santos and E. Kaxiras, ACS nano **7**, 10741 (2013).
[10] Z. Zhu, S. Carr, D. Massatt, M. Luskin, and E. Kaxiras, Phys. Rev. Lett. **125**, 116404 (2020).
[11] J. M. Soler, E. Artacho, J. D. Gale, A. García, J. Junquera, P. Ordejón, and D. Sánchez-Portal, Journal of Physics: Condensed Matter **14**, 2745 (2002).
[12] Y. Zhang and W. Yang, Phys. Rev. Lett. **80**, 890 (1998).
[13] M. Dion, H. Rydberg, E. Schröder, D. Langreth, and B. Lundqvist, Phys. Rev. Lett. **95**, 109902 (2005).
[14] G. Román-Pérez and J. M. Soler, Phys. Rev. Lett. **103**, 096102 (2009).
[15] K. Lee, É. D. Murray, L. Kong, B. I. Lundqvist, and D. C. Langreth, Phys. Rev. B **82**, 081101 (2010).
[16] J. Klimeš, D. R. Bowler, and A. Michaelides, Journal of Physics: Condensed Matter **22**, 022201 (2009).
[17] V. R. Cooper, Phys. Rev. B **81**, 161104 (2010).
[18] K. Berland and P. Hyldgaard, Phys. Rev. B **89**, 035412 (2014).
[19] O. A. Vydrov and T. Van Voorhis, The Journal of chemical physics **133**, 244103 (2010).
[20] J. Neugebauer and M. Scheffler, Phys. Rev. B **46**, 16067 (1992).
[21] L. Bengtsson, Phys. Rev. B **59**, 12301 (1999).
[22] L. N. Kantorovich, Phys. Rev. B **60**, 15476 (1999).
[23] B. Meyer and D. Vanderbilt, Phys. Rev. B **63**, 205426 (2001).
[24] J. Jung, A. M. DaSilva, A. H. MacDonald, and S. Adam, Nature communications **6**, 1 (2015).
[25] N. N. Nam and M. Koshino, Phys. Rev. B **96**, 075311 (2017).
[26] H. Yu, G.-B. Liu, J. Tang, X. Xu, and W. Yao, Science advances **3**, e1701696 (2017).
[27] Y. Frenkel, Phys Z Sowietunion **13**, 1 (1938).
[28] O. M. Braun and Y. S. Kivshar, Physics Reports **306**, 1 (1998).
[29] W. L. McMillan, Phys. Rev. B **14**, 1496 (1976).
[30] L. Bulaevski and D. Khomski, Zh. Eksp. Teor. Fiz **74**, 1863 (1978).
[31] V. Pokrovskiĭ and A. Talapov, Soviet Journal of Experimental and Theoretical Physics **48**, 579 (1978).
[32] A. M. Popov, I. V. Lebedeva, A. A. Knizhnik, Y. E. Lozovik, and B. V. Potapkin, Phys. Rev. B **84**, 045404 (2011).
[33] I. V. Lebedeva, A. V. Lebedev, A. M. Popov, and A. A. Knizhnik, Phys. Rev. B **93**, 235414 (2016).
[34] I. V. Lebedeva and A. M. Popov, The Journal of Physical Chemistry C **124**, 2120 (2019).
[35] I. V. Lebedeva and A. M. Popov, Phys. Rev. B **99**, 195448 (2019).